EPJ Web of Conferences **134**, 03001 (2017) DOI: 10.1051/epjconf/201713403001
Subnuclear Structure of Matter: Achievements and Challenges

Photoproduction of Mesons

Hartmut Schmieden[1,⋆] and *Friedrich* Klein[1,⋆⋆]

[1] *Physikalisches Institut, Universität Bonn*

Abstract. B.1 is one of the experimental projects within the CRC 16. It aims at the systematic investigation of the photoproduction of mesons off nucleons in order to understand reaction mechanisms and the relevant degrees of freedom in resonance formation. Of particular interest is the photoproduction of mesons heavier than the pion and resonances involving hidden or open strangeness. Essential hardware contributions have been made to the experimental programme of the CRC 16 through tagging systems, and photon-beam polarisation and polarimetry. A new experiment has been set up within the framework of the BGO-OD collaboration. This combines a forward magnetic spectrometer with a central BGO calorimeter with charged particle recognition and identification. The BGO-OD experiment enables reconstruction of complex final states composed of both charged and neutral particles, complementary to the existing CBELSA/TAPS calorimeter which is optimised for multi-photon final states. Selected results of the 12-year CRC period are presented from both experiments.

1 Introduction

The goal of CRC 16 project B.1 is the systematic investigation of the photoproduction of mesons off nucleons. Meson production is tightly connected with the nucleon excitation spectrum. Those gross features seem understood in terms of the quark sub-structure, but important aspects still remain puzzling.

In relation to constituent quark models and also recent results in Lattice-QCD [1], a large fraction of the expected excited states, predominantly at higher masses, remains "missing" in experiments [2]. Results in the double-strange sector of Ξ-hyperon states even seem to exacerbate the situation: Despite the expected improved separability of resonances due to smaller widths in the 2s-sector, almost no excited states at all are observed in photoproduction experiments [3].

Not only the higher states, also the lowest excitations in the non-strange and 1s-sector exhibit peculiar patterns, which are not described in genuine 3-quark models:
– Parity is reversed between the two lowest lying N^* excitations, $P_{11}(1440)$ with $J^P = 1/2^+$ and $S_{11}(1535)$ with $J^P = 1/2^-$; naturally the lowest state above the ground state would be expected to have negative parity, and the state above this to have positive parity.
– Mass is reversed between the two lowest lying negative parity states in the strange and non-strange sector, i.e. the $\Lambda(1405)$ and the $S_{11}(1535)$; naturally the state containing the s-quark would be expected heavier.[1]

These, and other patterns opened speculations regarding the inner structure of the states and the effective degrees of freedom, which are not necessarily just quarks. Due to the closeness of the chiral symmetry breaking scale to the nucleon mass/size scale, the associated Goldstone bosons also enter as effective "elementary" objects [4, 5], enabling interactions of the light mesons directly with quarks, and the formation of meson-baryon[2] type objects. Corresponding models indeed appear more successful than genuine three constituent quark models in some aspects, for example, determining the parity ordering of the lowest nucleon excitations [5]. Meson-baryon dynamics seem to play an important role for higher baryon excitations too [6–14]. In addition to the interaction of pseudoscalar mesons with baryons, vector mesons should also contribute to resonance formation [15–17]. In this case, degenerate states of $J^P = 1/2^-, 3/2^-$ are expected, in particular in the mass region around 2 GeV [18].

Meson-baryon dynamics may be expected to be particularly important at thresholds, for example through (sub-threshold) rescattering effects. Many unresolved structures seem associated with such production or decay thresholds, as is illustrated in Fig. 1. The above mentioned $\Lambda(1405)$ and $S_{11}(1535)$ lie directly at the $\bar{K}N$ and ηp thresholds, respectively. Around 1680 MeV at the closely spaced $\bar{K}\Sigma$ and ωp thresholds, a narrow peak structure is observed in η-photoproduction off the neutron [19–21]. This seems associated with a dip structure off the proton at the same energy, in particular at forward η angles [22], and a pronounced structure in the photon beam asymmetry off the proton at central angles [23]. In the ϕp photoproduction channel, an unexpected narrow peak is observed in the vicinity of the almost degenerate $K^*\Lambda_{g.s.}$ and $K^+\Lambda(1520)$ thresholds [24–26]. And, finally, a dip structure was found

⋆ e-mail: schmieden@physik.uni-bonn.de
⋆⋆ e-mail: klein@physik.uni-bonn.de

[1] despite the special role of the $\Lambda(1405)$ as the *uds*-singlet state

[2] in the meson sector also meson-meson

at the $K^*\Sigma$ threshold in $K_s^0\Sigma^+$ photoproduction off the proton, which is particularly pronounced at forward directions [27]. At the same energy, a structure is suggested in the photon beam asymmetry at central angles [28]. A dip in the cross section can be reproduced in a model based on vector meson-baryon interactions [29]. It appears associated with the formation of a $N^*(2030)$ vectormeson-baryon resonance, possibly in combination with a close-by $N^*(2080)$, and it is predicted to be complemented by a peak structure in $K_s^0\Sigma^0$ photoproduction off the neutron. This issue is not experimentally resolved yet. The phenomenology may be potentially similar to the situation in the η-channel at 1680 MeV.

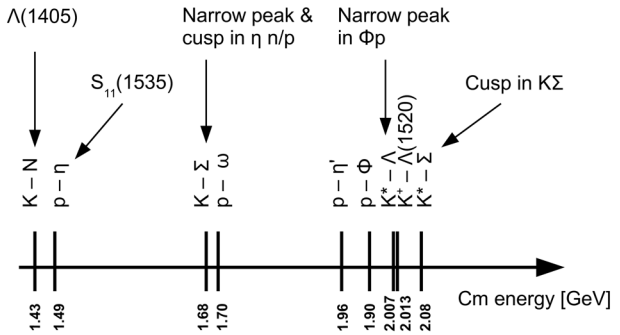

Figure 1: Overview of production/decay thresholds.

Some of the states which persistingly resisted a conventionial three-quark explanation are likely to be "dynamically" generated through meson-baryon interactions, at least to some extent. For the $\Lambda(1405)$ the important role of meson-baryon dynamics was recently supported by a result from LQCD [30]. Approaching realistic quark masses in the calculations, the $\Lambda(1405)$ seems to adopt a pronounced meson-baryon structure.

To better understand these issues, non-pionic channels are of particular interest. For the ELSA experiments this means η, associated K-hyperon and vectormeson photoproduction. The main goal is to disentangle the reaction mechanisms, in order to understand the excitations or structures observed. This is complementing projects preferentially pursuing spectroscopy of states. The results provide qualitative input and quantitative contraints for Partial Wave Analyses, for example, with respect to s versus t-channel contributions. In turn, the feedback from spectroscopy and PWA aids the interpretation of the data, and is also in tight cooperation with theory.

An essential aspect of the experiments are polarisation degrees of freedom. For the CBELSA/TAPS experiment, which is run in combination with the Bonn Frozen Spin polarised target, linearly polarised tagged photon beams and the necessary electron polarimetry for circularly polarised beam were provided. This is described in the next section.

The CBELSA/TAPS calorimeter setup, optimised for neutral final states which involve multiple photons, is complemented by the new BGO-OD experiment. Combining a large aperture magnetic spectrometer in forward directions with a central BGO ball, BGO-OD is ideal for reconstructing complex final states including both charged and neutral particles. This makes it especially suited for the strangeness and vectormeson channels addressed. Setup and commissioning results are described in section 3. Some selected results are then discussed in section 4.

2 Tagging and Polarimetry at the CBELSA/TAPS Experiment

The photon tagging system is an essential feature of the CBELSA/TAPS experiment. This includes the positioning system to align a diamond crystal to produce linearly polarised coherent bremsstrahlung, and a Møller polarimeter for in-situ measurements of the longitudinal electron beam polarisation. The latter provides the basis to determine the (energy-dependent) degree of circular polarisation of the photon beam.

2.1 Photon Tagging and Linear Polarisation

Energy tagging of bremsstrahlung photon beams is a common method in meson photoproduction experiments. The principle is to measure the momentum of the post-bremsstrahlung electrons using a magnetic spectrometer, and associate it with the detected hadronic reaction through time coincidences.

The electron beam extracted from the ELSA accelerator [31] impinges on one of a set of four amorphous copper radiators of thickness 15 – 300 μm (corresponding to 1.05 – 21 ‰ radiation lengths X_0), a diamond crystal for coherent bremsstrahlung of thickness 500 μm (4.1 ‰ X_0), or a magnetisable ferromagnetic foil[3] of effective thickness 58.5 μm (3.6 ‰ X_0) for in-situ Møller measurements when using a polarised electron beam. The radiators are accurately positioned by means of a commercial goniometer system.[4]

A schematic overview of the tagging system is shown in Fig. 2. The post-bremsstrahlung electrons are horizon-

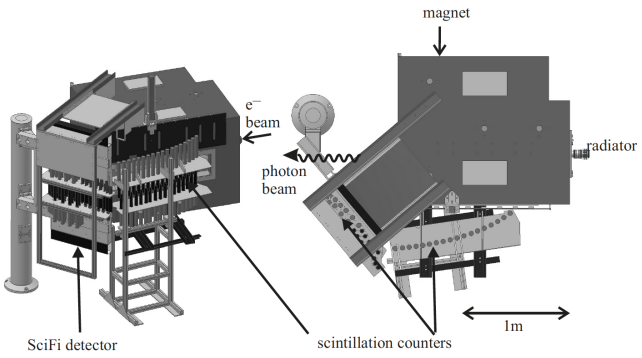

Figure 2: Schematics of the tagging system, 3-dimensional view (left) and top-view (right).

[3] material "Vacoflux", an alloy of 49 % iron, 49 % cobalt, and 2 % vanadium

[4] Newport Corporation *www.newport.com*

tally bent in the field of a *Brown-Boveri* MC type dipole magnet. Maximum field strength is 2 T at a current of 1500 A. Nominal settings are such that electrons of primary beam energy are deflected by 9 degree into the exit beamline and the electron beam dump. The momentum of the post-bremsstrahlung electrons is analysed through a two-part hodoscope of 96 half overlapping plastic scintillators. The backward part is placed in the focal plane of the magnet, against which the forward part had to be tilted due to space limitations. All scintillators are 1 cm thick, with the height and width varying from 6 – 13 cm and 1.4 – 5 cm, respectively. The total tagged photon energy range is from 21 % – 87.1 % E_0. Resolutions are between 0.1 % in electron energy for the lowest energy electrons and 0.4 % for the highest energies, which translates into a photon energy resolution of $\Delta E_\gamma/E_\gamma = 0.1...6.0\,\%$. The scintillator hodoscope is augmented by a 480 channel scintillating fibre (SciFi) detector. Arranged in two layers the 2 mm diameter fibres cover the high electron range of the tilted hodoscope part (cf. Fig. 2). In this range the photon energy resolution is significantly improved to $\Delta E_\gamma/E_\gamma < 2.9\,\%$. Setup, calibration and performance of the tagging system are described in detail in Ref. [32].

Linearly polarised photon beams are generated by coherent bremsstrahlung off the diamond radiator. Precise alignment through the goniometer system enables the setting of the energy range of maximum polarisation (the "coherent peak") and the orientation of the polarisation plane. The energy-dependent degree of polarisation can be determined from the energy spectrum of post-bremsstrahlung electrons. Methods and results are described in Ref. [33].

2.2 Circular Polarisation and Møller Polarimetry

Circularly polarised photon beams are obtained using a longitudinally polarised electron beam. The photon polarisation $P_\gamma(E_\gamma)$ is energy dependent, with the polarisation transfer from an electron beam of polarisation P_e given by [34]

$$P_\gamma/P_e = x\,\frac{3+(1-x)}{3+3(1-x)^2-2(1-x)}, \qquad (1)$$

where $x = E_\gamma/E_e$ is the fractional energy transfer, which is measured with the tagging system. The determination of P_γ requires the additional measurement of the degree of electron polarisation. This is done using a Møller polarimeter integrated into the tagging system.

In Møller scattering, a count rate asymmetry $A_M = (N^{++} - N^{+-})/(N^{++} + N^{+-})$ is obtained between parallel (++) and antiparallel (+−) spin orientations of the electrons which translates into

$$A_M = a_{zz} P_z^B P_z^T, \qquad (2)$$

where P_z^B and P_z^T are the longitudinal beam and target polarisations, and a_{zz} is the asymmetry coefficient, which follows from the Møller cross section and can be calculated in QED. For highly relativistic electrons it is energy independent. It does, however, depend on the Møller scattering angle with a maximum of $|a_{zz}| = 7/9$ for the symmetric case ($\theta^{cm} = 90$ degree) where, in the laboratory frame, both outgoing electrons have the same scattering angle and the same momentum $p'_e = p_0/2$, i.e. half the incoming beam momentum, p_0.

Due to the electron spin precession in magnetic (bending) fields, it is important to measure the polarisation of the electron beam directly at the nominal bremsstrahlung radiator position. This is easily achieved by simultaneously using the bremsstrahlung radiator as the Møller target. To determine the asymmetry according to Eq. 2, the target/radiator electrons need to be polarised. This is achieved by using one of the above mentioned ferromagnetic Vacoflux foils as the bremsstrahlung radiator. It is placed inside a small solenoid producing a magnetic field of approximately 0.008 mT, sufficient to magnetise the foil into saturation. The magnetisation of the foil is measured by inductive methods, and the electron polarisation determined using the gyromagnetic ratio. For Vacoflux the latter is known with a precision of $\simeq 0.7\%$.

The polarisation is orientated within the foil plane.[5] Therefore, target polarisation in exactly z – i.e. beam – direction can not be realised. Instead, the foil is slightly tilted against the beam direction, in our case by 20 degree. The (unwanted) small sensitivity induced by this for transverse components of the beam polarisation is compensated for by alternate tilt settings of +20 and −20 degree, which sign-flip and thus cancel the measured transverse components in the asymmetry while leaving the longitudinal one unaffected.

The polarimeter tags Møller scattering events through coincident detection of the two outgoing electrons in a pair of lead glass detectors of thickness 6.4 cm. Lead plates of 1 cm thickness in front of the detectors ensure the shower maximum to lie inside the detector material for the symmetric scattering case at the magic[6] beam energy of 2.4 GeV. To minimise systematic errors through the Levchuk effect [35], symmetric scattering is selected through momentum. The detectors are accordingly arranged after the tagger dipole, and behind the tagger scintillator strip and fibre hododcopes. The plane for Møller pairs to be detected is chosen perpendicular to the bending plane of the tagger magnet. This allows to place the detectors far enough from the magnet's mid plane, thus avoiding the high rate exposition through post-bremsstrahlung electrons.

The polarimeter works fast enough to be used for accelerator diagnostics. At nominal tagger rates of a few MHz a relative statistical error of $(\delta P_e/P_e)_{stat} \simeq 2\%$ is achieved after about 15 minutes, the precision of which can be increased with longer data taking periods. The overall limitation is always the total systematic error of $(\delta P_e/P_e)_{syst} \simeq 1.5\%$ which is dominated by the precision of the target foil polarisation. A detailed description of beam polarimetry for the CBELSA/TAPS experiment can be found in Ref. [36].

[5] To magnetise a thin foil perpendicular to its plane requires a much larger external field exceeding the saturation field of $B_{sat} \simeq 2.25$ T, and would require, for example, superconducting magnets to produce it.

[6] At this energy the electron spin orientation is exactly longitudinal at the radiator position

3 BGO-OD

The BGO-OD experiment emerged from the B.1 project of a magnetic spectrometer, originally intended to be used in combination with Crystal Barrel to detect forward going charged particles with high resolution over a large acceptance. The main device is a 94 t large-aperture dipole magnet[7], the "open dipole" (OD). A major part of the former GRAAL group joined the spectrometer project, which led to the formation of the international BGO-OD collaboration in March 2010 with currently 62 members of institutions from Basel University, Bonn University (HISKP and PI), Edinburgh University, INFN Frascati, PNPI Gatchina, Gießen University, Kharkov University, Messina University and INFN, Moscow University, Pavia University and INFN, Rome "Tor Vergata" and INFN, and Torino University and INFN. In particular the Italian groups contribute very significantly to the BGO-OD experiment, most importantly through the 480 channel BGO ball which was previously used at the ESRF Grenoble and is now installed with upgraded electronics at ELSA.

The photon tagging system at BGO-OD works upon the same principles as the system in operation at the CBELSA/TAPS experiment (see section 2.1). Linearly polarised photon beams are available via coherent bremsstrahlung using a diamond radiator [37]. To determine the accuracy of extracting the degree of polarisation, beam asymmetries were determined for both $p\eta$ and $p\pi^0$ final states. The data agreed well with previous data sets and model fits (see [37] for details).

Circularly polarised photon beams are produced using longitudinally polarised electron beams from ELSA. A Møller polarimeter is used to determine the degree of circular polarisation [38].

The BGO ball encloses the cryogenic target[8] over the angular range from 25°–155°, complemented by detectors for charge recognition and tracking[9] (see Fig. 3). Forward directions are covered by the OD spectrometer (see Fig. 4). The magnet is sandwiched by tracking detectors and complemented by a time-of-flight (TOF) spectrometer. The small acceptance gap between the BGO ball and forward spectrometer is covered with a segmented plastic scintillator detector, labelled SciRi in Fig. 3. This acceptance gap will also be covered by a special MRPC[10] (labelled Daisy in Fig. 3), which is presently under construction at Rome. Generally, the BGO-OD setup is ideally suited for unpolarised target experiments with complex final states including both charged and neutral mesons, hence ideal to pursue associated strangeness and vector meson production.

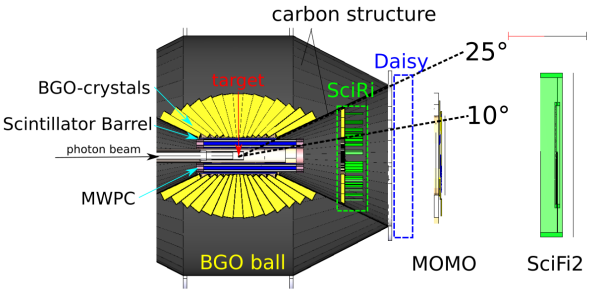

Figure 3: A slice view through the BGO ball.

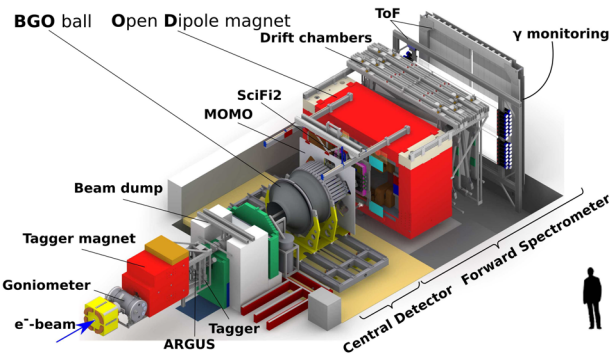

Figure 4: A schematic of the BGO-OD experiment.

The commissing of BGO-OD was succesfully finished in 2015. Additionally to commissioning tests, the first data of approximately 25 days with linearly polarised photon beams was taken during 2015. A small subset of this data is shown in Figs. 5 and 6. Fig. 5 shows the reconstruction of neutral mesons in the BGO ball. With timing cuts applied to ensure a coincidence between the tagged beam photons and events recorded in the BGO, the mass recoiling from two photons in the final state is plotted against the invariant mass of the two photons. Peaks corresponding to the $p\pi^0$ and $p\eta$ final state are visible. The two photon invariant mass for a selection of events where the the mass recoiling from the mesons is consistent with the proton mass is shown in Fig. 5(b).

Fig. 6 shows the same subset of data for particle trajectories reconstructed in the forward spectrometer. Fig. 6(a) shows, for postively charged particles, β (calculated from the time of flight walls), plotted against momentum (calculated from the extent of curvature of the particle trajectory in the magnetic field of the open dipole). Enhancement of events for π^+ and protons are seen to agree well with the expected loci denoted by the red lines. Of these events, a subset was selected where the forward going particle is likely to be a proton. The mass recoiling from the proton in the final state is plotted in Fig. 6(b). Peaks consistent with η, ω and η' mesons are visible without further analysis.

[7] We thank DESY for providing the magnet on permanent loan basis.
[8] Provided by Messina university and INFN.
[9] A cylindric MWPC is being built by the Pavia group.
[10] Multi resistive plate chamber

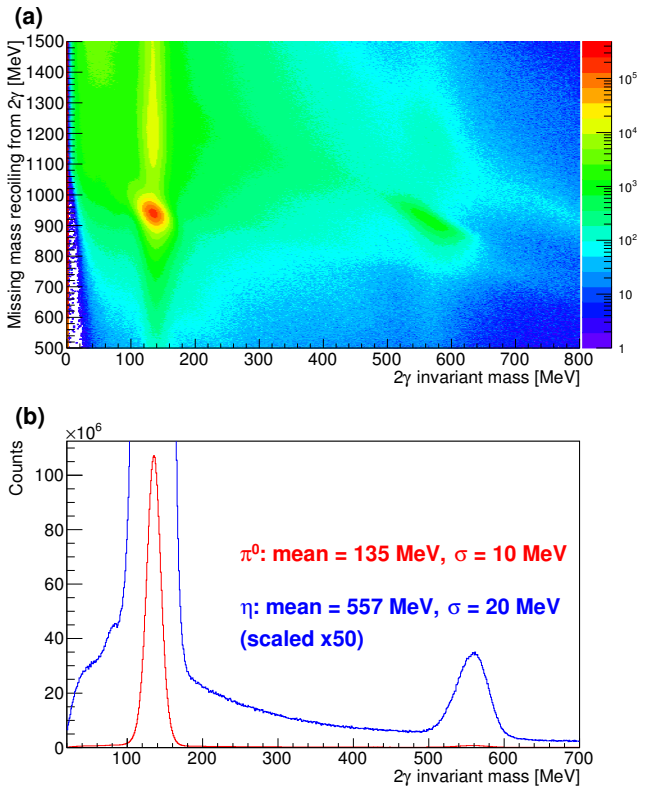

Figure 5: Neutral meson reconstruction in the BGO. (a) Mass recoiling from a two photon system versus the two photon invariant mass. (b) Two photon invariant mass after a selection cut where the mass recoiling from the two photon system is within 2σ of the proton mass. The mean and sigma values are from a Gaussian fit to the π^0 and η invariant mass peaks (red and blue respectively). To observe the η mass peak, the data is replotted and scaled by a factor of 50.

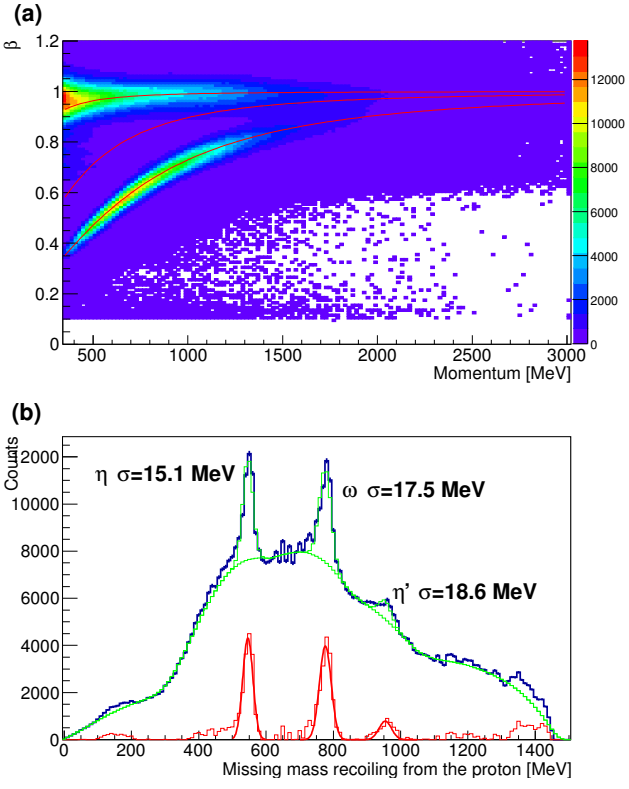

Figure 6: Positively charged particle reconstruction in the forward spectrometer. (a) Particle β versus momentum. Red lines indicate the expected loci of π^+, K^+ and protons. (b) The mass recoiling from forward going protons (thick dark blue line). The green line was used to estimate background and extract the peaks at the η, ω and η' masses (red lines). The peaks were subsequently fitted with a Gaussian function (thick red curves), the widths of which are labelled inset.

Additionally to commissioning tests and the liquid hydrogen target data that was taken, approximately two days of data with a carbon target, and two days of data with a liquid deuterium target were taken during 2015.

4 Selected Results

As motivated in section 1, a particular interest is the photoproduction of mesons beyond the pion, and to disentangle reaction dynamics at reaction thresholds. The CBELSA/TAPS detector essentially comprises a highly segmented 4π electromagnetic calorimeter, optimised for multi-photon final states. Therefore, neutral mesons were detected in their neutral decay modes, e.g. $\eta \to \gamma\gamma$ or $\to 3\pi^0 \to 6\gamma$, $\omega \to \pi^0\gamma \to 3\gamma$, $K^0_s \to \pi^0\pi^0 \to 4\gamma$.

Polarisation observables play an important role in understanding the photoproduction mechanism. The most basic one is the beam asymmetry, Σ, which is accessible through linearly polarised photon beams, and provides seed for a whole class of double polarisation observables which are sensitive to aspects of spin-orbit interactions involved [39].

The new BGO-OD detector opens a window to more complex final states of mixed neutral and charged particles. First preliminary results are presented including $K^+Y^{(*)}$ with subsequent decay of the (excited) hyperons into different channels. Charged mesons not only can be detected in the magnetic forward spectrometer, but also in the central BGO calorimeter, using the inner scintillator barrel and MWPC as vetoes (section 3). This includes K^+ detection in the BGO using the time delayed weak decay as explained in section 4.4.1.

A few personal-choice selected results of the last 12 year CRC/TR-16 funding are presented in the following.

4.1 Beam asymmetry in ηp photoproduction

As described in Ref. [40], the beam asymmetry was measured in the reaction $\vec{\gamma}\, p \to \eta\, p$ using linearly polarised tagged photon beams from coherent bremsstrahlung, which is described in section 2.1. By accurate alignment

of the diamond crystal the coherent peak was set to the energy range $E_\gamma = 800 - 1400$ MeV. A maximum polarisation of $P_\gamma = 49\%$ was obtained at $E_\gamma = 1305$ MeV. The η was detected in both dominant decay modes, $\eta \to 2\gamma$ and $\eta \to 3\pi^0$, and the beam asymmetry extracted from the azimuthal modulation of the cross section [41],

$$\frac{d\sigma}{d\Omega} = \left(\frac{d\sigma}{d\Omega}\right)_0 \left[1 - P_\gamma \Sigma \cos 2\Phi\right]. \quad (3)$$

Large asymmetries of up to 80% were extracted over a cm angular range of $\Theta_\eta^{cm} = 50 - 150$ degree. It was shown that with both the eta-MAID model and the Bonn-Gatchina partial wave parametrisation the measurement could be described equally well, although their relative resonance contributions differed substantially. This is illustrated in Fig. 7, and was mainly traced back to the interplay of $P_{11}(1710)$ and $P_{13}(1720)$, and $D_{13}(1520)$ and $D_{15}(1675)$ states. These results clearly demontrated the need to measure further double-polarisation observables, in order to resolve such an unsatisfactory situation.

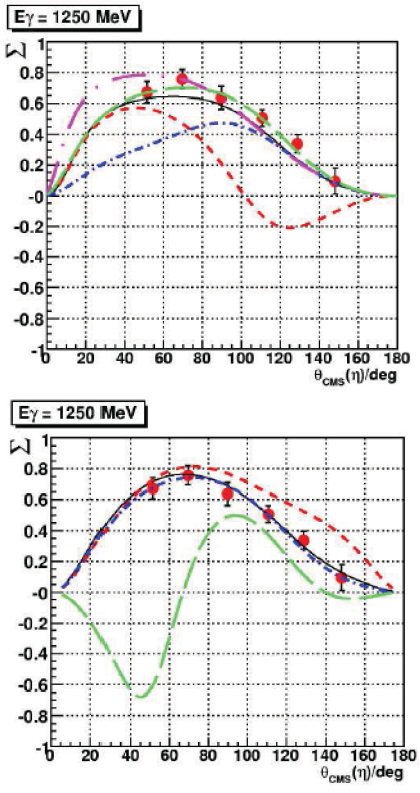

Figure 7: Impact of different resonance contributions to the beam asymmetry in η – *MAID* (left) and the Bonn-Gatchina PWA (right), both plotted at a photon beam energy of 1250 MeV. Full lines represent full calculations, broken curves the effect of "turning off" individual resonances: $P_{13}(1720)$ (long dashed), $P_{11}(1710)$ (long dash-dotted), $D_{13}(1520)$ (short dashed), and $D_{15}(1675)$ (short dash-dotted). The figure is taken from Ref.[40].

4.2 Measurements of polarisation observables and spin-density matrix elements in ω-meson photoproduction

ω photoproduction is an ideal channel to explore the lesser known third resonance region due to the higher production threshold compared to pionic channels. Furthermore, the isoscaler nature of the ω ($I = 0$) allows only N^* states to contribute to the reaction mechanism, with no interference from Δ resonance states.

For vector meson photoproduction, at least 23 polarisation observables are required to completely determine the photoproduction amplitudes and relative phases, which is considerably more than the eight required for pseudoscalar meson photoproduction. Despite this, the measurement of only a few polarisation observables provides important insights into the reaction mechanism. The data presented here are from three papers. Klein et al. [42] measured photon beam asymmetries, Σ, and pion asymmetries, Σ_π, for ω photoproduction close to threshold. Eberhardt et al. measured the beam-target helicity asymmetries, E, G and G_π from threshold [43], and Wilson et al. the differential cross sections and spin-density matrix elements [44].

At higher energies, ω photoproduction is dominated by diffractive scattering, via the exchange of a Pomeron, as shown in Fig. 8, top. π exchange, as depicted in Fig. 8, centre, should also be expected due to the sizable observed decay mode $\omega \to \pi^0\gamma$ ($\Gamma = 8.3\%$). The energy and angular dependence of the differential cross section near threshold however cannot be described with these mechanisms alone. Previous beam asymmetries from GRAAL [45], supported the significance of s-channel resonances near threshold (Fig. 8, bottom). A study of ω photoproduction at CLAS [46, 47], via the decay $\omega \to \pi^+\pi^-\pi^0$ was made after the paper described here by Klein et al. [42], but before the paper by Eberhardt et al. [43]. Strong evidence for several N^* states were found, including $N(1680)5/2^+$, $N(1700)3/2^+$ and $N(2190)7/2^+$.

The measurement of polarisation observables is particularly sensitive to the role of s-channel resonances near threshold. The beam asymmetry, Σ, is expected to be close to zero for pure t-channel mechanisms, but large with s-channel contributions. This can be explained by the manner of the photon coupling: If the photon couples to the vector meson, and with no angular momentum transferred in the t-channel (either for Pomeron or pion exchange), no beam asymmetry should be observed. Conversely, the observable Σ_π, which is a measurement of the extent of the asymmetry in the decay $\omega \to \pi^0\gamma$, is predicted to be +0.5 or -0.5 for pure Pomeron and pion exchange respectively. From existing partial wave analyses, significant contributions from s-channel mechanisms should render Σ_π close to zero. The simultaneous measurement of Σ and Σ_π as was made in [42] will therefore constrain the role of the three mechanisms close to the ω threshold.

The measurements of E, G and G_π that were made in [43] also act to understand the photoproduction mechanism close to threshold. For Pomeron or pion exchange, E should be zero. E may be non-zero for a mixture of the two exchange mechanisms. For s-channel contributions, E

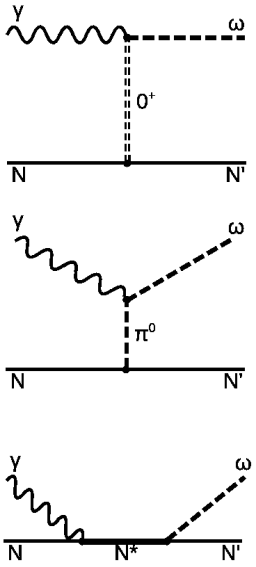

Figure 8: ω production via t-channel 0^+ (Pomeron) exchange (top), t-channel π^0 exchange (middle) and s-channel intermediate resonance (bottom).

will be the projection of the intermediate state spin upon the beam axis.

Based on the unpolarised cross section and the photon beam asymmetry, spin-density matrix elements were determined for the reaction $\gamma p \to p\omega$ using the radiative decay $\omega \to \pi^0\gamma$ [44]. The cross sections cover the full angular range, yielding shape of the angular distribution and unpolarised spin-density matrix elements in agreement with previous data. In the energy range E_γ = 1150 – 1650 MeV polarised spin-density matrix elements were extracted for the first time using the radiative channel. The data were included in the Bonn-Gatchina partial wave analysis.

The measurements with unpolarised and linearly polarised photon beams [42–44] used an electron energy of 3.2 GeV from ELSA [31]. The electrons were incident upon a diamond radiater, 500 μm thick, and aligned to produce linearly polarised photons via the coherent bremsstrahlung process. For the measurement of E presented in [43], a longitudinally polarised electron beam with an energy of 2.4 GeV was also used to produce a circularly polarised photon beam. The electrons were incident upon a Møller radiator to produce bremsstrahlung photons and simultaneously determine the degree of polarisation (see section 2.2).

The $\omega \to \pi^0\gamma$ channel was observed using the Crystal Barrel [48] and TAPS [49, 50] detector system. Surrounding the target was a three layer scintillating fibre detector [51] for charged particle identification and reaction vertex determination. For the measurement of Σ presented in [42], a liquid hydrogen target was used. For the measurements of E, G and G_π presented in [43], a 2 cm long, longitudinally polarised butanol target was used [52].

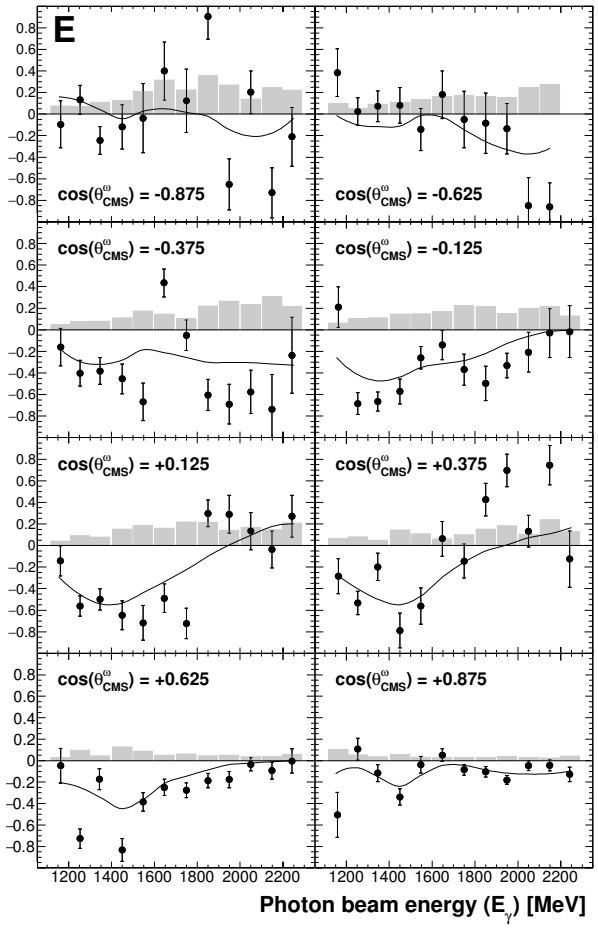

Figure 9: $p\omega$ Beam-target-helicity asymmetry, E, as a function of photon beam energy. Systematic errors are on the abscissa. The solid line is the result of the Bonn-Gatchina PWA when including this data. Figure taken from [43].

Fig. 9 shows the E measurement from the analysis of Eberhardt et al. [43]. The overlayed line is the solution from a Bonn Gatchina partial wave analysis, using a large body of data, including this data set. The fit found significant contributions from Pomeron exchange, particularly at higher energies, but only a small contribution from pion exchange. Intermediate s-channel resonances were found to be important, with significant contributions from a $J^P = 3/2^+$ and $J^P = 5/2^+$ states below 1.9 GeV, and an improvement with the additional inclusion of a $J^P = 3/2^-$. Table 1 [53] details the changes the new data sets have in constraining the resonance contribution in ω photoproduction.

Fig. 10 shows the Σ and Σ_π measurements of Klein et al. [42]. It was noted that there is a dependence of Σ on the centre of mass polar angle. Given the extent of the variation away from zero, this was considered as evidence of s-channel mechanisms playing a significant role. This is supported by the Σ_π measurement, which remains close to zero. A further comparison to Bonn-Gatchina PWA, which did not include this data set, showed that s-channel

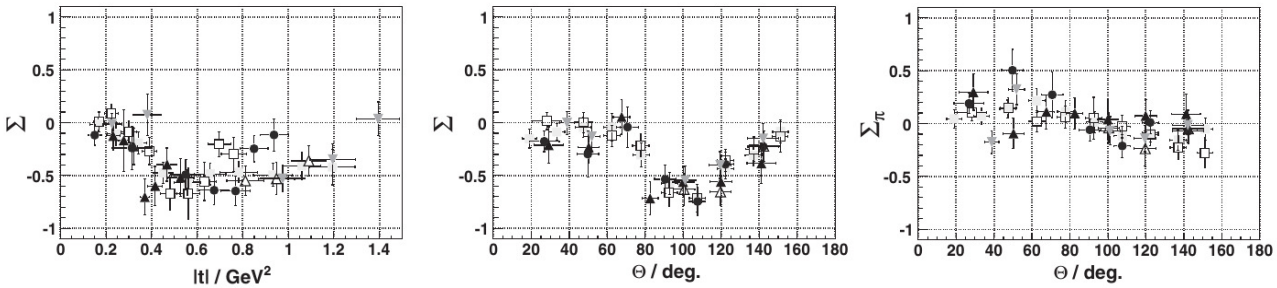

Figure 10: Photon beam asymmetries and pion asymmetries for beam energies 1108-1200 MeV (black triangles), 1200-1300 MeV (open squares), 1300-1400 MeV (black circles), 1400–1500 MeV (open triangles), and 1500–1700 MeV (grey triangles). Figure taken from [42].

resonances are required to have a satisfactory fit to the data.

Resonance	B.R.	$\delta(\chi^2)$	Resonance	B.R.	$\delta(\chi^2)$
$N(1700)3/2^-$	22 ± 12	100	$N(1900)3/2^+$	15 ± 8	70
				13 ± 9	
$N(1710)1/2^+$	2 ± 2	26	$N(2000)5/2^+$	18 ± 8	42
	8 ± 5			1 ± 1	
$N(1720)3/2^+$	26 ± 14	105	$N(2060)5/2^-$	4 ± 3	37
$N(1875)3/2^-$	13 ± 7	98	$N(2100)1/2^+$	15 ± 10	78
	20 ± 4				
$N(1880)1/2^+$	20 ± 8	33	$N(2150)3/2^-$	12 ± 8	99
$N(1895)1/2^-$	28 ± 12	100	$N(2190)7/2^-$	14 ± 6	131

Table 1: Branching ratios for N^* contributions to $N\omega$. $\delta\chi^2$ is the change in χ^2 with the inclusion of the new data. Taken from [53].

There is a change of sign of E at 1650 MeV at $\cos\theta^{\omega}_{CMS} = 0.125$, and a peak like structure at -0.375 and -0.125. This is interesting as it is the region of the cusp-like structure in the $K^0_s\Sigma^+$ cross section over the K^* threshold [27], which is described in the following subsection.

4.3 Differential cross section and polarisation observable measurements for $K^0_s\Sigma^+$

In the strange quark sector, K^0_s photoproduction is an ideal tool to understand the effective degrees of freedom that are required to model excitation spectra. Compared to charged K^+ photoproduction, few measurements of K^0_s photoproduction have been made. This channel benefits from the lack of the t-channel kaon exchange mechanism, as the photon cannot couple to the vanishing charge of the neutral K^0. On the contrary, K^0_s photoproduction is sensitive to t-channel K^* exchange. Detailed measurements of K^0_s photoproduction over the K^* thresholds therefore allow an understanding of the role of t-channel exchange, and potentially, K^*-hyperon dynamically generated interactions which may contribute to the K^0_s photoproduction process.

The data presented here are from differential cross section measurements of $\gamma p \rightarrow K^0_s\Sigma^+$ from threshold to a photon beam energy of 2250 MeV [27], and the first recoil polarisation and beam asymmetry measurements made for this reaction channel [28].

Both experiments were performed at the Crystal Barrel [48] and TAPS [49, 50] detector system. An electron beam energy of 3.2 GeV was extracted from ELSA [31]. This was incident upon a 500 μm diamond radiator, which was orientated to produce linearly polarisated photons via the coherent bremsstrahlung process, with peaks in the photon energy spectrum at 1305, 1515 and 1814 MeV. The photon beam was incident upon a 5.3 cm long liquid hydrogen at the centre of the Crystal Barrel. The absolute photon flux was determined by a fast, total absorbing lead tungstate crystal detector behind the TAPS detector.

Simulated $\gamma p \rightarrow K^0_s\Sigma^+$ data was used to determine the detection efficiency when identifying the reaction channel via the decays $K^0_s \rightarrow 2\pi^0$ and $\Sigma^+ \rightarrow \pi^0 p$. This was found to be flat across the entire polar angle range, with an efficiency of approximately 11% near threshold, and reducing to 2% in the highest energy bin of 2150 to 2250 MeV.

Fig. 11 shows the differential cross section, for both with and without the requirement of the charged cluster from the proton detection. There is good agreement between the data sets. Previous data from Crystal Barrel [54] and SAPHIR [55] are also shown, which agree reasonably well with this new data.

Near threshold, the cross section is approximately flat, with respect to the centre of mass polar angle. This is expected for a dominantly s-wave production mechanism. With increasing beam energy, the differential cross section becomes more forward peaked, indicative of t-channel mechanisms becoming more dominant. This continues up to a beam energy of 1750 MeV. In the energy bin 1750 to 1850 MeV, the cross section sharply drops at forward angles by a factor of approximately four. At higher energies, the cross section remains flat at approximately 0.02 μb/sr. The cusp-like structure is so pronounced that it is visible in the total integrated cross section shown in Fig. 12.

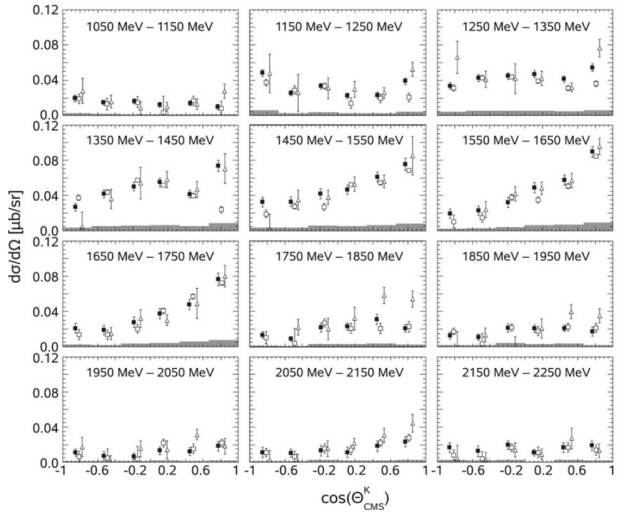

Figure 11: $\gamma p \rightarrow K^0_s\Sigma^+$ differential cross sections. Filled squares are this data (grey bars on the abscissa are the systematic errors), open squares are the previous data from the Crystal Barrel [54], and the open triangles are the previous data from SAPHIR [55]. Figure taken from [27].

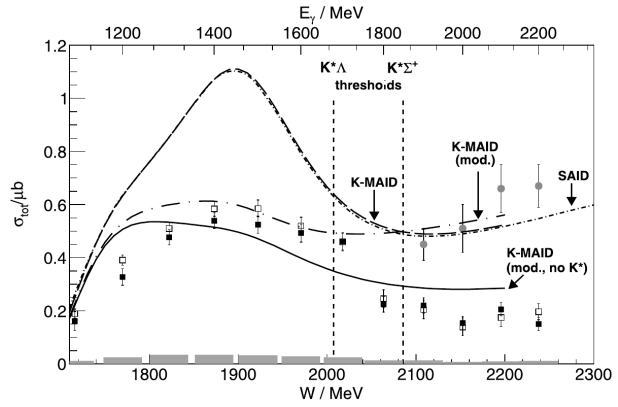

Figure 12: Total $\gamma p \rightarrow K^0_s\Sigma^+$ cross sections. Filled squares are this data (grey bars on the abscissa are the systematic errors), open squares are the previous data from the Crystal Barrel [54]. Grey circles are the addition of this data to $K^{*0}\Sigma^+$ cross section data of Nanova et al. [58]. The SAID [56] and modified Kaon Maid (K-MAID) [57] solutions which are labelled inset are described in the text. Figure taken from [27].

The exhibited behaviour suggests there is a t-channel mechanism that contributes below 1750 MeV, but not above this energy, leaving only s-channel contributions as the dominant mechanism. To test this hypothesis, the SAID [56] solution, and modified versions of the Kaon-MAID calculation [57] are overlayed in fig 12. Using the standard parameterisation, neither SAID nor Kaon-MAID can fit the data below a beam energy of 1700 MeV. An improvement can be made however by manually adjusting the couplings of the $S_{31}(1900)$ state to $G_1 = 0.3$ and $G_3 = 0.3$, and a reduction of the Born couplings to 0.7. Fig. 12 shows this adjusted fit, and an additional fit without the K^* exchange term. The inclusion of the K^* exchange term improves the description of the data below the K^* threshold, but the omission of this term gives an improved description above this energy. The grey data points show this data summed with the $K^{*0}\Sigma^+$ total cross section data of Nanova et al. [58]. The incoherent addition of this data shows an agreement with the modified Kaon-MAID solution when K^* exchange terms are included. This suggests that K^* channels contribute to the $K^0_s\Sigma^+$ cross section below K^* threshold. Above threshold, K^* is produced on-shell and therefore no longer contributes to the $K^0_s\Sigma^+$ cross section.

It is speculated that the mechanism shown in Fig. 13 is responsible for this cusp-like structure. A K^* is produced off-shell, and subsequently rescatters to a K^0_s and π, where the π is absorbed by the hyperon. The coupled channel model by Ramos and Oset, which includes vector meson-baryon interactions, supports this claim [29]. An interesting prediction of this model is a peak like structure in the $K^0_s\Sigma^0$ cross section in photoproduction off the neutron. Measurements of this channel will therefore provide further constraints to meson-baryon interactions and are intended at the BGO-OD experiment.

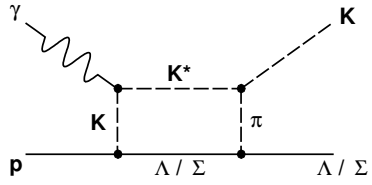

Figure 13: t-exchange diagram for K^0_s photoproduction, with an intermediate K^0_s and pion rescattering through sub-threshold K^* decay.

Fig. 14 shows the photon beam asymmetry for $K^0_s\Sigma^+$ photoproduction. In general there is better agreement with the Bonn-Gatchina PWA solution than any of the modified Kaon-MAID parameterisations. An improved variant of the Bonn-Gatchina PWA was included, which used in the fit the $K^0_s\Sigma^+$ data presented here. The new fit suggested a significant $J^P = 3/2^-$ contribution over a large energy range. A larger contribution of $J^P = 3/2^-$ than $J^P = 3/2^+$ gave a better fit to the beam asymmetry data, however the opposite was true for the recoil polarisation data.

At the most forward angle and high energy bin ($\cos\theta^{cm}_K = 0.8$, $E_\gamma = 1550$ MeV), the photon beam asymmetry deviates from the trends described by the Bonn Gatchina PWA, and has a negative value of -0.7. This is an interesting region as it is just below the K^* thresholds and the cusp-like structure that was observed in the differential cross section. Extension of beam asymmetry and recoil polarisation measurements over this energy region will be possible with the BGO-OD experiment.

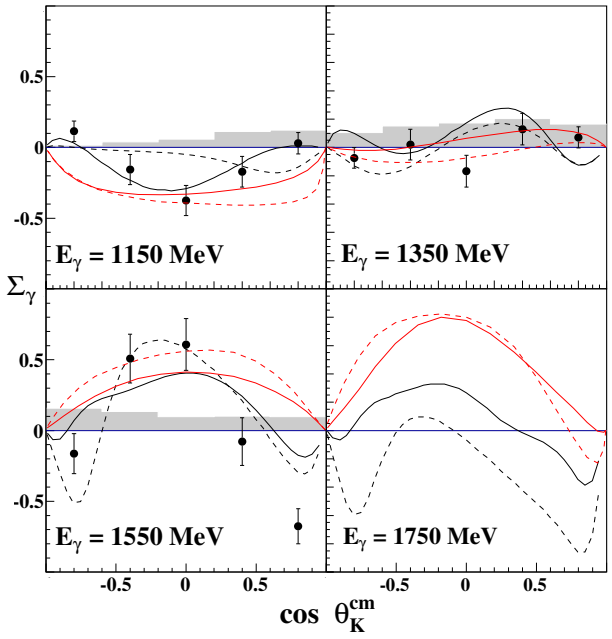

Figure 14: Angular distribution of the photon beam asymmetry Σ_γ in the three bins of photon energy indicated in the diagrams. The error bars attached to the data points are purely statistical, the systematic errors are indicated by the grey bars on the abscissa. Curves represent the results of the Bonn-Gatchina-PWA [59] solutions, BG2011-02m (black dashed) and BG2011-02 (black solid), and the K-MAID [57] parametrisations, standard (red solid) and modified as described in the text, to study the origin of the cross section anomaly at the K^* threshold (red dashed). The fourth energy bin is added to show the behaviour of the parametrisations across the K^* thresholds where there is no data yet available. Figure taken from [28].

4.4 Strangeness photoproduction at the BGO-OD experiment

BGO-OD is ideal for the investigation of reactions dominated by t-channel mechanisms, due to the acceptance at forward angles with high momentum resolution. Neutral particle identification in the central region aids the identification of final states of mixed charge. This unique combination is suited to the investigation of reaction channels with open strangeness and complicated final states.

The preliminary analysis presented in this section demonstrates the BGO-OD capabilities of reconstructing channels with both K^0_s and K^+ in the final state.

4.4.1 K^+ detection in the BGO ball

K^+ reconstruction over the polar angle range of the BGO is crucial to identify associated strangeness final states over a large kinematic range. The techniques presented here are currently being used to extract differential cross section data for $K^+\Lambda$ and $K^+\Sigma^0$ channels. This can be used to help resolve discrepancies in the world data set, in particular at $W \approx 1.9$ GeV, where differences in differential cross section data from SAPHIR [60] and CLAS [61, 62] leave ambiguities to the *s*-channel contributions.

Accurate understanding of K^+ detection in the BGO also is crucial for the measurements of channels with higher lying hyperons. It is intended to study, for example, differential cross sections and polarisation observables for $K^+\Lambda(1405)$ and $K^+\Lambda(1520)$. Measurements of $K^+\Lambda(1405)$ at BGO-OD will be complementary to recent measurements made at CLAS [63, 64]. BGO-OD is suited in particular to identify the decay $\Lambda(1405) \rightarrow \pi^0\Sigma^0$ via photon reconstruction in the BGO. This channel discriminates against the mass-overlapping $\Sigma(1385)$, for which it is isospin forbidden. Of course, K^+ reconstruction is also important for vector meson studies, for example $\gamma p \rightarrow p\phi$ with the subsequent decay $\phi \rightarrow K^+K^-$.

A technique of K^+ detection developed with the Crystal Ball detector [65] was implemented for the BGO ball [66]. It makes use of the weak decay of K^+ into the dominant modes $\mu^+\nu_\mu$ and $\pi^+\pi^0$ with time delays characteristic to the K^+ lifetime of approximately 12 ns. The BGO time resolution per crystal allows the K^+ cluster to be separated into an incident sub-cluster from stopping the K^+, and a decay sub-cluster from the subsequent decay. Fig. 15 shows a schematic of the technique and characteristic energy and time spectra. Fig. 15(b) shows the energy of the decay cluster with a peak at 153 MeV, corresponding to the μ^+ energy deposition when the K^+ decays via the $\mu^+\nu_\mu$ mode at rest. There is excellent agreement between real and simulated data. Events where the K^+ decays pionically are usually lost, since the two sub-clusters cannot be spatially separated. Fig. 15(c) shows the time difference between the incident subcluster from stopping the K^+, and the decay subcluster. The real and simulated spectra agree very well, and an exponential fit to the spectra yields a lifetime close to the expected K^+ lifetime of 12 ns.

Fig. 16 shows the mass recoiling from the K^+ in the final state for both real and simulated data. Peaks at the Λ, Σ^0 and $\Lambda(1405)$ or $\Sigma(1385)$ masses are visible. Events from $K^+\Sigma^0$ and $K^+\Lambda$ reaction channels can be separated by identifying the radiative $\Sigma^0 \rightarrow \Lambda\gamma$ decay [66]. A detection efficiency of the decay $\Sigma^0 \rightarrow \Lambda\gamma$ (having already identified the K^+) of approximately 50-60% is obtained, with misidentification of $K^+\Lambda$ events of less than 10%.

4.4.2 Kinematic fitting and neural network analysis

Kinematic fitting has been successfully implemented at the BGO-OD experiment, with careful analysis to understand energy and spatial resolution of particle momenta reconstruction. This has been used to reconstruct the reaction $\gamma p \rightarrow K^+\Sigma^0$ over a wide kinematic range [67]. The analysis shown here used the full set of liquid hydrogen target data that was taken during 2015.

The techniques described below are complementary to either detecting the K^+ in the forward spectrometer or in the BGO via the weak decay as described in section 4.4.1. The angular acceptance is however higher, and in particular for when the K^+ is detected in the BGO, the detection efficiency is greatly increased. These techniques have application in studying higher lying hyperons. For example,

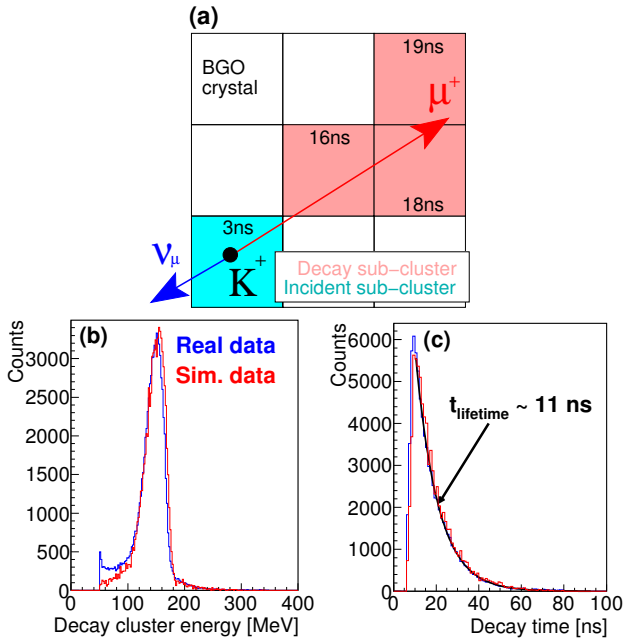

Figure 15: K^+ identification in the BGO ball. (a) An initial cluster is separated by time to an incident sub-cluster of crystals (blue) and decay sub-cluster (red). The time inset each crystal indicates the time of the measured energy deposition. (b) The energy of the decay sub-cluster. (c) The time difference between the incident sub-cluster from stopping the K^+, and the decay sub-cluster from the K^+ decay.

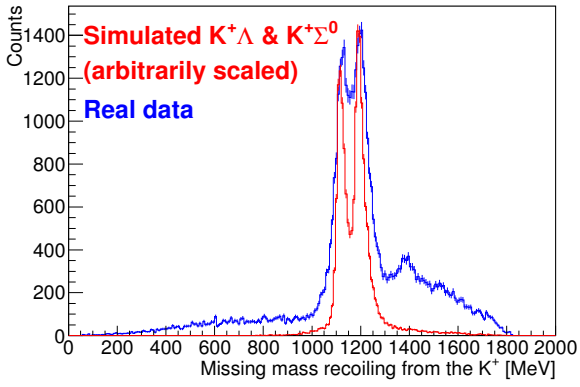

Figure 16: Missing mass recoiling from K^+ detected in the BGO. Blue line is real data, red line is simulated $K^+\Lambda$ and $K^+\Sigma^0$ final states, arbitrarily scaled with respect to each other and the real data.

$\gamma p \rightarrow K^+\Lambda(1405)$, via the decay $\Lambda(1405) \rightarrow \pi^0\Sigma^0$, can be studied in a similar manner, but with the additional reconstruction of the π^0 in the BGO ball.

Events were selected under the assumption that after the decay $\Sigma^0 \rightarrow \gamma\Lambda$, the Λ decayed to $p\pi^-$. It was therefore required to identify three charged particles over the

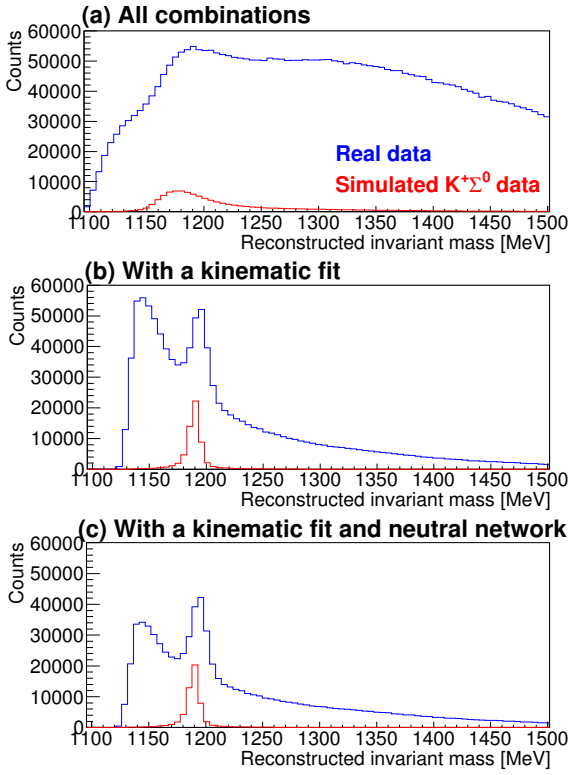

Figure 17: Identification of $K^+\Sigma^0$ via three charged particles in either the BGO, SciRi or the forward spectrometer, and a photon in the BGO [67]. The reconstructed Σ^0 invariant mass is plotted for real and simulated data (blue and red respectively) for (a) All combinations of selected events, (b) After a kinematic fit and a confidence level cut of 1%, and (c) after the kinematic fit and applying a neutral network to remove background.

range of the forward spectrometer, SciRi and BGO (where a coincidence with the inner plastic scintillator determined the particle charge), and an additional neutral cluster in the BGO. The momenta of the three charged particles were determined by requiring momentum conservation transverse to the beam (in the xy plane). The direction of the three particles is a sufficient constraint to determine their momenta, and energy signals from the detectors were not required. Three solutions per event were made, depending upon the order of assignment of the K^+, proton and π^- to the three detected charged particles. The beam energy was then used to determine the overall energy conservation for each solution, and the solution with the closest conserved energy was chosen. Fig. 17 shows the reconstructed Σ^0 invariant mass using this technique for real and simulated data. Fig. 17(a) is the results from the selection process described, with a broad bump at the Σ^0 mass, but with a large amount of background from misidentified events in the real data. Fig. 17(b) is the same event selection but with a kinematic fit applied. The contraints enforced by the fit were the Λ mass and total momentum conservation. A selection cut rejected events with a confidence level below 1%. A narrow peak is now visible at the Σ^0 mass

in real and simulated data. A neural network has been preliminarly implemented to understand the event topology and be able to distinguish true $K^+\Sigma^0$ final states from background. Fig. 17(c) shows the same event selection after the kinematic fit but with an additional selection cut to remove events which the neural network considered to be background. For real data, the integral of the background spectrum reduces, leaving the integral of peak corresponding to $K^+\Sigma^0$ events unchanged. The peak from simulated $K^+\Sigma^0$ remains unchanged.

Fig. 18 shows preliminary $\gamma p \rightarrow K^+\Sigma^0$ differential cross sections using this technique [67]. A complete, solid angle acceptance of 4π can be accessed with this technique, and with only approximately 25 days of data, it is clear that the statistics are comparable to previous measurements.

4.4.3 K^+ at forward angles

Despite the channels $K^+\Lambda$ and $K^+\Sigma^0$ having been extensively studied, there remains a dearth of data at extremely forward K^+ centre of mass polar angles. This region is crucial to understand the role of t channel mechanisms which are forward peaking and dominate the reaction process (see for example [70] and reference therein). Accurately knowing the free $\gamma p \rightarrow K^+\Lambda$ production cross section at forward angles is also an important constraint in hypernuclei electroproduction, where there is typically very small Q^2 and forward going K^+.

The data presented below are preliminary differential cross section for $\gamma p \rightarrow K^+\Lambda$, for K^+ travelling at extremely forward angles [38]. The analysis shown is approximately one third of the available liquid hydrogen target data set taken during 2015.

Due to to the comparatively low cross section of final states with associated strangeness, additional cuts are required to observe K^+ directly in β versus momentum plots for particles detected in the forward spectrometer. The requirement of a π^0 reconstructed in the BGO and a total BGO energy deposition of less than 250 MeV accentuates $K^+\Lambda$ and $K^+\Sigma^0$ final states where the forward going K^+ takes the majority of the available energy. Fig. 19(a) shows the β versus momentum plot with these cuts applied, with a visible loci corresponding to K^+. Particle mass was calculated from β and momentum and shown in Fig. 19(b). Events were selected where this mass was between 420 to 640 MeV, corresponding to a 1σ of a Gaussian fit to the K^+ mass peak. A deliberately narrow selection range was chosen to reduce background, however this range may be extended in future analysis. Fig. 20(a) shows the mass recoiling from the forward going K^+, with clear peaks corresponding to Λ and Σ^0. The same technique of identifying the photon from the decay $\Sigma^0 \rightarrow \gamma\Lambda$ that was described in section 4.4.1 was applied, and the $K^+\Sigma^0$ events removed. Fig. 20(b) shows the remaining spectrum, with a clear peak at the Λ mass.

A detection efficiency of between 10-20% was determined for K^+ detection at forward angles. This is limited by the proportion of K^+ which decay on flight and are therfore not identified. With the additional requirement of a

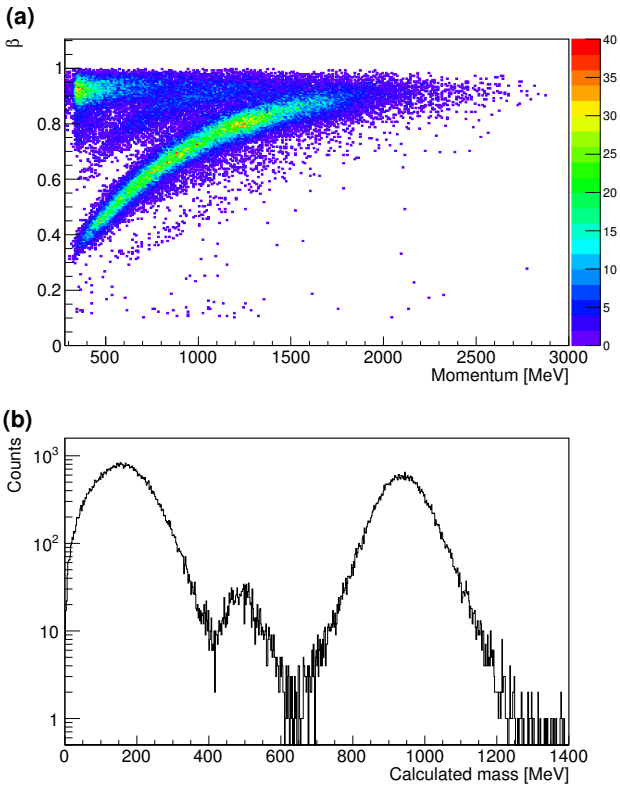

Figure 19: K^+ selection in the forward spectrometer. (a) β versus momentum for positively charged particles. To accentuate the loci of K^+ between the protons and π^+, a selection cut required an energy sum of less than 250 MeV in the BGO, and the decay $\Sigma \rightarrow \Lambda\gamma$ to be identified, as described in section 4.4.1. (b) Particle mass calculated from β and momentum.

π^0 in the BGO, the detection efficiency reduces to approximately 6%, due to the efficiency of π^0 reconstruction, and the decay branching ratio of $\Lambda \rightarrow \pi^0 n$ of 35.8%.

Fig. 21 shows preliminary $K^+\Lambda$ differential cross sections at forward angles for two W intervals. The data extends over a larger energy range, however further analysis is required at these intervals to separate signal from background. The data presented here is approximately 1/3 of the available data from 2015 and, nevertheless, the statistics are comparable to the previous data labelled in Fig. 21.

Removing BGO selection cuts (π^0 selection and energy sum) allows the identification of higher lying hyperon states via K^+ detection in the forward spectrometer [66]. Fig. 22(a) shows the mass recoiling from the K^+ under these conditions. Peaks corresponding to $\Sigma(1385)$ and $\Lambda(1405)$ (which need further analysis to separate), $\Lambda(1520)$, and potentially higher states up to 1800 MeV are visible. The event topology can be significantly changed by the requirement of additional charged particles and reconstructed π^0, as shown in Fig. 22(b,c,d). For example, the requirement of a π^0 and at least another charged particle (besides the K^+) accentuates the peak at the $\Sigma(1385)$ and $\Lambda(1405)$ masses, while the requirement of at least

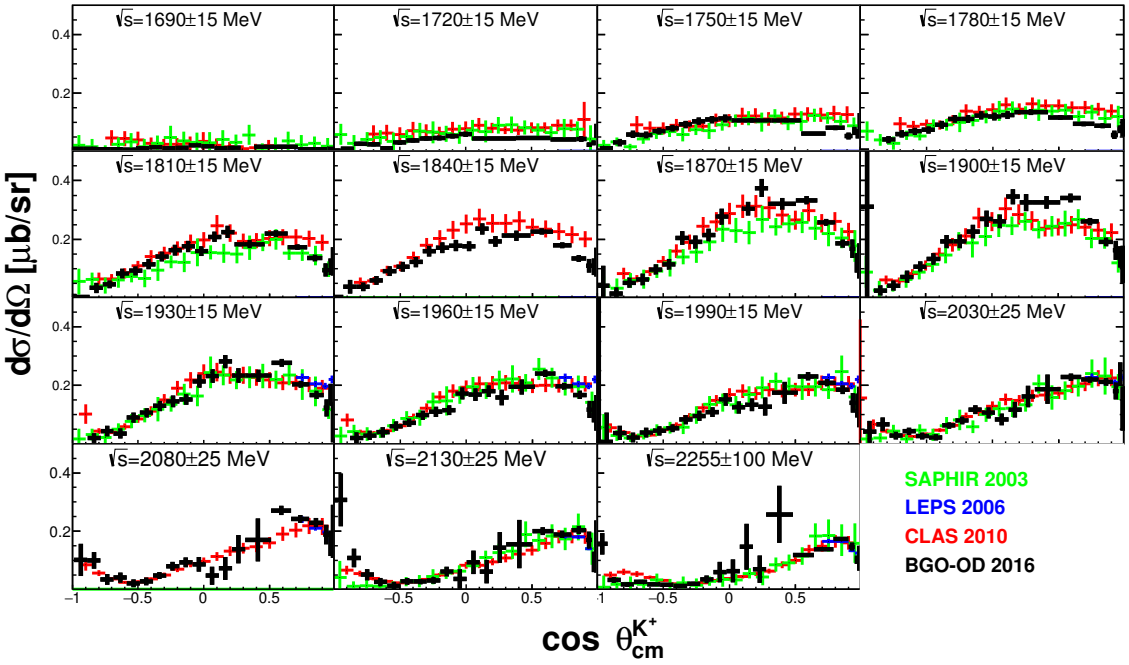

Figure 18: Preliminary $\gamma p \rightarrow K^+\Sigma^0$ differential cross section data versus the K^+ centre of mass polar angle. Centre of mass energy ranges, $\sqrt{s}$ labelled inset. Black points are this preliminary data [67], green are the SAPHIR data of Glander et al. [60], blue are the LEPS data of Sumihama et al. [68], and red are the CLAS data of Dey et al. [69].

two more charged particles accentuates the peak at the $\Lambda(1520)$ mass. Analysis to isolate particular K^+Y^* states is in progress.

4.4.4 K^0_s detection from a deuterium target

An important measurement to be made with BGO-OD is the $K^0_s\Sigma^0$ differential cross sections over the K^* threshold regions. As was described in section 4.3, the model of Ramos and Oset [29] uses vector meson-baryon interactions to describe $K^0_s\Sigma^+$ data. This model predicts a peak for $K^0_s\Sigma^0$ data at the K^* thresholds. Measurements over this region are therefore crucial in constraing meson - baryon degrees of freedom in the photoproduction mechanism.

Additionally to this measurement, studies of the reaction $\gamma n \rightarrow K^0_s Y$, give important insights and constraints into the reaction mechanism for associated strangeness photoproduction. The photoproduction of charged and neutral kaons are intrinsically related via SU(3) symmetry, leading to relations between hadronic coupling constants. This can be used, for example as shown in reference [71], for better constraints upon isobar models for both charged and neutral kaon photoproduction.

Data from a two day test beam with a liquid deuterium target has been used to demonstrate the K^0_s identification procedure in the pure neutral channel [72]. Analysis with simulated data demonstrated that there is significant background from channels with uncorrelated multiple π^0 in the final state. A selection cut demanding that no more than five neutral clusters should be identified in the BGO, and no more than two charged particles identified either in the BGO, SciRi or the forward spectrometer was used to suppress this background. After applying timing cuts between neutral clusters and the tagged photon beam, events were selected where the two π^0 could be reconstructed via pairs of photons with a combined invariant mass between 114 - 162 MeV. With the preliminary energy calibration used, this corresponded to approximately 2σ of a fitted Gaussian function to the π^0 mass peak.

Fig. 23(a) shows the $2\pi^0$ invariant mass after selecting events where the mass recoiling from the $2\pi^0$ system is consistent with the Σ^+ mass (1050 - 1250 MeV). A quadratic function was fitted to the background, with a Gaussian function fitted to the peak corresponding to the K^0_s mass. An additional method was used, where a proton or π^- was required in the forward spectrometer. Assuming the decay, $\Lambda \rightarrow p\pi^-$, the mass recoiling from the $2\pi^0 p$ or $2\pi^0\pi^-$ system should be the π^- or proton masses respectively. Events were selected consistent with this topology, and the resulting $2\pi^0$ invariant mass is shown in Fig. 23(b). The peak corresponding to the K^0_s mass is now more pronounced above the background, albeit with lower statistics.

The same analysis was performed with data using a liquid hydrogen target. No peak structure at the K^0_s mass was observed, however the background looked very similar. This suggests that the peak observed with the deuterium target was from the reactions $\gamma n \rightarrow K^0_s\Sigma^0$ and $\gamma n \rightarrow K^0_s\Lambda$. Due to limited statistics with the real data set, no serious attempt has been made to separate these two channels. Simulated data has shown however that the technique of identifying the photon from the decay $\Sigma^0 \rightarrow \Lambda\gamma$,

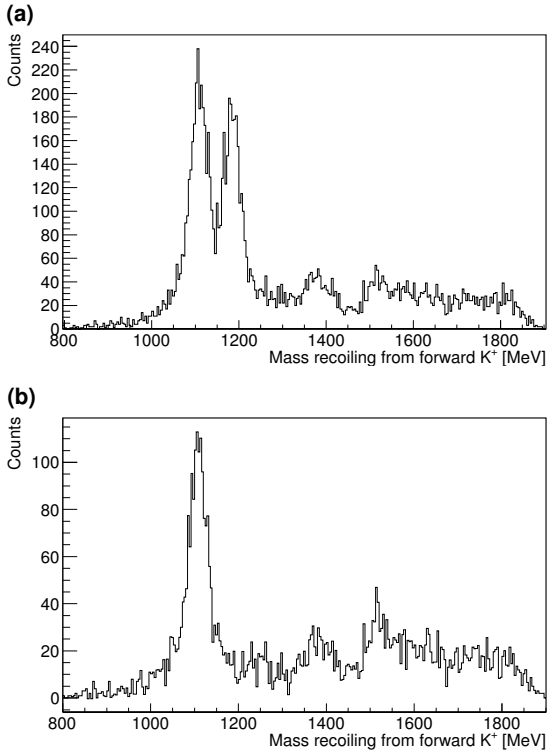

Figure 20: Mass recoiling from forward going K^+. (a) To accentuate the peaks corresponding to the Λ and Σ^0 hyperons, a selection cut required an energy sum of less than 250 MeV and for a π^0 to be identified in the BGO. (b) $K^+\Sigma^0$ events were identified as described in section 4.4.1, and removed, leaving a pronounced peak from the $K^+\Lambda$ final state.

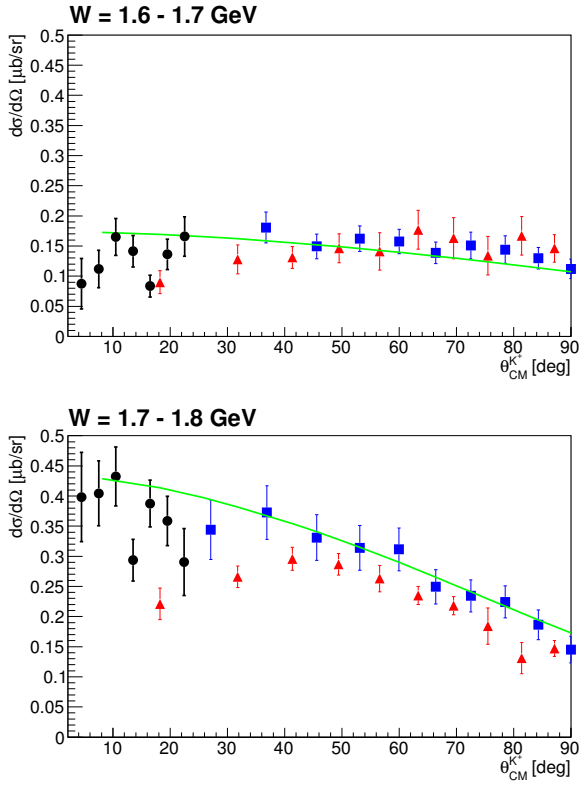

Figure 21: $\gamma p \rightarrow K^+\Lambda$ differential cross sections. Black circular data are from this analysis, at a preliminary stage [38]. Blue squares and red triangles are the data of McCracken (CLAS) [62] and Glander (SAPHIR) [60] respectively. The green line is the current parameterisation from Bonn - Gatchina PWA.

as was described for K^+ detection in section 4.4.1, will work for these channels as well.

5 Summary and Outlook

The goal of project B.1 was the systematic investigation of the photoproduction of mesons off nucleons in order to understand the reaction mechanisms involved, and the relevant degrees of freedom in resonance formation. Of particular interest were mesons heavier than the pion, for example η, ω and K^0_s, and resonances carrying hidden or open strangeness. Polarisation is an important tool, and essential hardware contributions have been made to the experimental programme of the CRC 16 in this regard. As a requirement for the experiments, photon tagging systems have been designed and set up for the CBELSA/TAPS and BGO-OD experiments. Both include coherent bremsstrahlung radiators for linearly polarised photon beams and Møller polarimeters to determine the energy dependent degree of circular polarisation when a polarised electron beam is used. Using polarised photon beams in conjunction with the Bonn polarised frozen spin target, significant results could be achieved in single and double polarisation experiments which, in combination with the unpolarised cross section measurements, provided essential input for partial wave and other theoretical analyses. Selected highlights are the single and double polarisation measurements in ω-photoproduction which helped to disentangle the reaction mechanism near threshold, and to identify specific s-channel resonances involved. In the strange sector, a cusp like structure was observed in $K^0_s\Sigma^+$ production at the K^* threshold which in chiral unitary models seems to be associated with one or two dynamically generated vector meson-baryon states around 2 GeV.

In the frame of the BGO-OD collaboration a new experiment has been set up. It combines a forward magnetic spectrometer with a central BGO calorimeter with charged particle recognition and identification. The BGO-OD experiment enables reconstruction of complex final states composed of both charged and neutral particles, complementary to the existing CBELSA/TAPS calorimeter which is optimised for multi-photon final states. The experiment was commissioned at the end of the CRC period and first physics data were taken. The preliminary results demonstrate the performance of the detector. It opens a new experimental window to investigate hadronic excitation structures, complementary

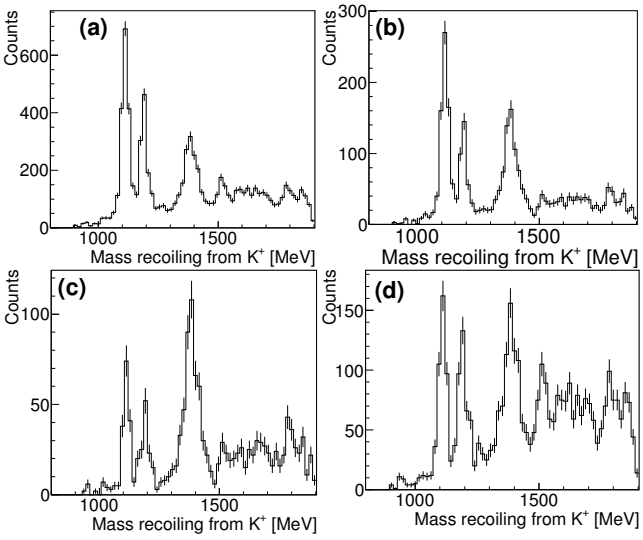

Figure 22: Missing mass recoiling from a forward K^+ over a momentum range of 500 - 800 MeV, with different selection criteria: (a) All data. (b) With a π^0 reconstructed in the BGO. (c) With a π^0 reconstructed and at least one additional charged particle. (d) With at least two additional charged particles.

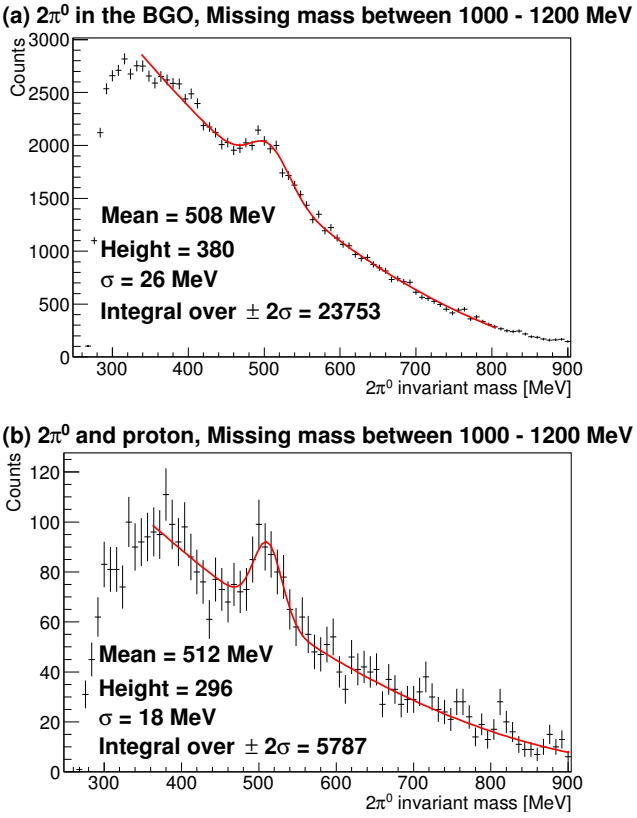

Figure 23: K^0_s detection with a deuterium target (approximately two days of data taking). Selection cuts described in the text enhanced the $\gamma n \to K^0_s \Sigma^+$ signal above background. (a) The invariant mass of $2\pi^0$ after selecting events where the missing mass is consistent with either the Λ or Σ^0 masses. (b) The invariant mass of $2\pi^0$ after selecting events where the missing mass from the $2\pi^0 p$ system is consistent with the π^- mass (assuming the decay $\Lambda \to p\pi^-$). For both histograms, a second order polynomial and a Gaussian function describe the background and K^0_s signal respectively. Parameters from the fitted Gaussian function are inset.

to other experiments and facilities.

The results presented by the spokespersons of B.1 are the fruits of work and commitment of numerous people involved in the project over the past 12 years. Many students who received their Bachelor's, Master's, or Diploma degrees significantly contributed to the success of B.1. In particular, the doctoral students carried the main load of technical developments and data analysis. Without their enthusiasm the whole project would have been unthinkable. Equally important have always been the postdoctoral fellows with their dedication to B.1. Particular mention for their contributions deserve Daniel Elsner, Jürgen Hannappel, Thomas C. Jude, and Valentina Vegna. As co-spokesperson during the first 4-year funding period Hartmut Kalinowsky made important contributions in the initial phase of B.1.

For providing excellent beam we thank the whole staff of the ELSA accelerator, in particular the technical director Wolfgang Hillert. The project also benefited from the support of the mechanical and electronics workshops. We thank DESY for providing the BGO-OD spectrometer magnet on permanent loan basis, and the IPN Orsay for loan of the TOF detector of the former GRAAL experiment. Very signifcant contributions to the BGO-OD experiment by Italian Universities and INFN in the frame of the BGO-OD collaboration are gratefully acknowledged, as is the fruitful co-operation with PNPI Gatchina and INR Moscow.

The whole work reported here would not have been possible without the continuous support from the Land Northrine-Westphalia, and from the Deutsche Forschungsgemeinschaft within the SFB/TR (CRC) 16, which we are very grateful for.

References

[1] R. Edwards et al., Phys. Rev **D 84** (2011) 074508

[2] E. Klempt and J.M. Richard, Rev. Mod. Phys. **82** (2010) 1095

[3] L. Guo et al. (CLAS collaboration), Phys. Rev **C 76** (2007) 025208

[4] A. Manohar and H. Georgi, Nucl. Phys. **B 234** (1984) 189

[5] L.Ya. Glozman and D.O. Riska, Physics Reports **268** (1996) 263

[6] R.H. Dalitz and J.G. McGinley, in *Low and Intermediate Energy Kaon-Nucleon Physics*, ed. by E. Ferrari and G. Violini, Reidel, Boston (1981) 381; R. H. Dalitz, T.C. Wong, and G. Rajasekaran, Phys. Rev. **153** (1967) 1617

[7] P.B. Siegel, and W. Weise, Phys. Rev **C 38** (1988) 2221

[8] N. Kaiser, T. Waas, and W. Weise, Nucl. Phys, **A 612** (1997) 297

[9] C. Garcia-Recio, M.F.M. Lutz, and J. Nieves, Phys. Lett B 582 (2004) 49
[10] M.F.M. Lutz and E.E. Kolomeitsev, Phys. Lett. **B 585** (2004) 243
[11] B. Borasoy, P.C. Bruns, U.-G. Meißner and R. Nißler, Eur. Phys. J. **A 34** (2007) 161
[12] P.C. Bruns, M. Mai, U.-G. Meißner, Phys. Lett. **B 697** (2011) 254
[13] J.A. Oller and U.-G- Meißner, Phys. Lett. **B 500** (2001) 263
[14] B. Borasoy, U.-G. Meißner and R. Nißler, Phys. Rev **C 74** (2006) 055201
[15] P. Gonzalez, E. Oset and J. Vijande, Phys. Rev **C 79** (2009) 025209
[16] S. Sarkar et al., Eur. Phys. J. **A 44** (2010) 431
[17] E. Oset and A. Ramos, Eur. Phys. J. **A 44** (2010) 445
[18] E. Oset et al., AIP Conf.Proc. 1388 (2011) 295, arXiv:1103.0807v1 [nucl-th]
[19] V. Kuznetsov et al., Phys. Lett. **B 647** (2007) 23
[20] I. Jaegle et al., Phys. Rev. Lett. **100** (2008) 252002
[21] I. Jaegle et al., Eur. Phys. J. **A 47** (2011) 89
[22] E.F. McNicoll et al., Phys. Rev **C 82** (2011) 035208; Erratum: Phys. Rev **C 84** (2011) 029901
[23] V. Kuznetsov and M.V. Polyakov, JETP Letters **88** (2008) 347, and V. Kuznetsov et al., Acta. Phys. Polon. **39** (2008) 1949 and references therein
[24] T. Mibe et al., Phys. Rev. Lett. **95** (2005) 182001
[25] B. Dey et al., Phys. Rev **C 89** (2014) 055208
[26] H. Seraydaryan et al., Phys. Rev **C 89** (2014) 055206
[27] R. Ewald et al., Phys. Lett. **B 713** (2012) 180
[28] R. Ewald et al., Phys. Lett. **B 738** (2012) 268
[29] A. Ramos and E. Oset, Phys. Lett. **B 727** (2013) 287
[30] J.M.M. Hall et al., Phys. Rev. Lett. **114** (2015) 132002
[31] W. Hillert, Eur. Phys. J. **A 28**, s01 (2006) 139
[32] K. Fornet-Ponse, Doctoral Thesis, Physikalisches Institut, Bonn (2009)
[33] D. Elsner et al., Eur. Phys. J. **A 39** (2009) 373
[34] H. Olsen and L.C. Maximon, Phys. Rev **114** (1959) 887
[35] L.G. Levchuk, Nucl. Instr. Meth. **A 345** (1994) 496
[36] S. Kammer, Doctoral Thesis, Physikalisches Institut, Bonn (2010)
[37] A. Bella, Doctoral Thesis, Physikalisches Institut, Bonn (2016)
[38] T. Zimmermann, Doctoral Thesis, Physikalisches Institut, Bonn (2016)
[39] H. Schmieden, Chinese Physics **33** (2009) 1146
[40] D. Elsner et al., Eur. Phys. J. **A 33** (2007) 147
[41] G. Knöchlein, D. Drechsel, L. Tiator, Z. Phys. **A 352** (1995) 327
[42] F. Klein et al., Phys. Rev. **D 78** (2008) 11
[43] H. Eberhardt, T.C. Jude, H. Schmieden et al., Phys. Lett. **B 750** (2015) 453
[44] A. Wilson et al., Phys. Lett. **B 749** (2015) 407
[45] J. Ajaka et al., Phys. Rev. Lett. **96** (2006) 132003
[46] M. Williams et al., Phys. Rev. **C 80** (2009) 065208
[47] M. Williams et al., Phys. Rev. **C 80** (2009) 065209
[48] E. Aker et al., Nucl. Instrum. Methods **A 321** (1992) 69
[49] R. Novotny et al., IEEE Trans. Nucl. Sci. **38** (1991) 379
[50] A. R. Gabler et al., Nucl. Instrum. Methods **A 346** (1994) 168
[51] G. Suft et al., Nucl. Instr. Meth. **A 538** (2005) 416
[52] Ch. Bradtke, H. Dutz et al., Nucl. Instr. Meth. **A 436** (1999) 430
[53] I. Denisenko et al., Phys. Lett. **B 755** (2016) 97
[54] R. Castelijns, et al., Eur. Phys. J. **A 35** (2008) 39
[55] R. Lawall, et al., Eur. Phys. J. **A 24** (2005) 275
[56] R.A. Arndt, et al., http://gwdac.phys.gwu.edu
[57] http://www.kph.uni-mainz.de/MAID/ (version 29.3.2007)
[58] M. Nanova, et al., Eur. Phys. J. **A 35** (2008) 333
[59] A. V. Anisovich et al., Eur. Phys. J. **A 47** (2011) 27
[60] K.H. Glander et al., Eur. Phys. J. **A 19** (2004) 251
[61] R. Bradford, R. A. Schumacher et al., Phys. Rev. **C 73** (2006) 035202
[62] M. E. McCracken, M Bellis, C. A. Meyer, M. Williams et al., Phys. Rev. **C 81** (2010) 025201
[63] K. Moriya, R. A. Schumacher et al., Phys Rev **C 87** (2013) 035206
[64] K. Moriya, R. A. Schumacher et al., Phys. Rev. Lett. (2014) 082004
[65] T.C. Jude, D.I. Glazier, D.P. Watts *et al.*, Phys. Lett. **B 735** (2014) 112
[66] T.C. Jude et al., JPS Conf. Proc. **10** (2016) 032002
[67] G. Scheluchin, Doctoral Thesis, Physikalisches Institut, Bonn (in preparation)
[68] M. Sumihama et al., Phys. Rev. **C 73** (2006) 035214
[69] B. Dey et al., Phys. Rev. **C 82** (2010) 025202
[70] D. Skoupil and P. Bydžovský, Phys. Rev. **C 93** (2016) 025204
[71] T. Mart, Phys. Rev. **C 83** (2011) 048203
[72] T.C. Jude et al., priv. comm. (2016)